



# Crustal Magnetic Fields Do Not Lead to Large Magnetic-field Amplifications in Binary Neutron Star Mergers

Michail Chabanov<sup>1</sup> , Samuel D. Tootle<sup>1</sup> , Elias R. Most<sup>2,3,4</sup> , and Luciano Rezzolla<sup>1,5,6</sup> <sup>1</sup> Institut für Theoretische Physik, Goethe Universität, Max-von-Laue-Str. 1, D-60438 Frankfurt am Main, Germany<sup>2</sup> Princeton Center for Theoretical Science, Princeton University, Princeton, NJ 08544, USA<sup>3</sup> Princeton Gravity Initiative, Princeton University, Princeton, NJ 08544, USA<sup>4</sup> School of Natural Sciences, Institute for Advanced Study, Princeton, NJ 08540, USA<sup>5</sup> Frankfurt Institute for Advanced Studies, Ruth-Moufang-Str. 1, D-60438 Frankfurt am Main, Germany<sup>6</sup> School of Mathematics, Trinity College, Dublin 2, Ireland

Received 2022 November 30; revised 2023 January 25; accepted 2023 February 14; published 2023 March 3

## Abstract

The amplification of magnetic fields plays an important role in explaining numerous astrophysical phenomena associated with binary neutron star mergers, such as mass ejection and the powering of short gamma-ray bursts. Magnetic fields in isolated neutron stars are often assumed to be confined to a small region near the stellar surface, while they are normally taken to fill the whole star in numerical modeling of mergers. By performing high-resolution, global, and high-order general-relativistic magnetohydrodynamic simulations, we investigate the impact of a purely crustal magnetic field and contrast it with the standard configuration consisting of a dipolar magnetic field with the same magnetic energy but filling the whole star. While the crust configurations are very effective in generating strong magnetic fields during the Kelvin–Helmholtz-instability stage, they fail to achieve the same level of magnetic-field amplification of the full-star configurations. This is due to the lack of magnetized material in the neutron-star interiors to be used for further turbulent amplification and to the surface losses of highly magnetized matter in the crust configurations. Hence, the final magnetic energies in the two configurations differ by more than 1 order of magnitude. We briefly discuss the impact of these results on astrophysical observables and how they can be employed to deduce the magnetic topology in merging binaries.

*Unified Astronomy Thesaurus concepts:* [Neutron stars \(1108\)](#); [Magnetars \(992\)](#); [Magnetic fields \(994\)](#); [Magnetohydrodynamical simulations \(1966\)](#); [Magnetohydrodynamics \(1964\)](#)

## 1. Introduction

The coincident detection of the gravitational-wave signal GW170817, of the short gamma-ray burst GRB 170817A, and of the kilonova AT2017gfo (Abbott et al. 2017; Cowperthwaite et al. 2017; Drout et al. 2017) has provided strong evidence that short gamma-ray bursts are related to binary neutron star (BNS) mergers and that magnetic fields play an important role in the postmerger evolution. This conclusion stems from a series of studies identifying magnetic fields as crucial to generate magnetically driven outflows (Kiuchi et al. 2012; Siegel et al. 2013; Kiuchi et al. 2018; Fernandez et al. 2019; Cioffi 2020a; Fujibayashi et al. 2022) but also to produce the conditions necessary for jet formation and launching (Anderson et al. 2008; Liu et al. 2008; Rezzolla et al. 2011; Palenzuela et al. 2013; Kiuchi et al. 2015b; Murguía-Berthier et al. 2016; Cioffi 2020b; Nathanail et al. 2020, 2021; Gottlieb et al. 2022).

Early studies identified that turbulence, starting from the Kelvin–Helmholtz instability (KHI) triggered in the first few milliseconds after merger by the shearing of the stellar surfaces, is essential in the amplification of the magnetic field (Price & Rosswog 2006; Giacomazzo et al. 2011; Kiuchi et al. 2015a; Aguilera-Miret et al. 2020). However, because the accurate description of the turbulent motions can only be achieved at enormous computational cost, a number of suggestions have been made over the years to obtain a subgrid-scale modeling of

the magnetic-field evolution. These so-called “large-eddy simulations” (LESs) have attempted to incorporate the small-scale, dynamo-driven, magnetic-field amplification into *global* high-resolution general-relativistic magnetohydrodynamics (GRMHD) simulations employing computationally affordable resolutions (Giacomazzo et al. 2015; Palenzuela et al. 2015; Radice 2017; Aguilera-Miret et al. 2020). At the same time, *local* and high-resolution simulations of KHI-driven turbulence have shown evidence of possible converged and saturated magnetic-field amplification (see, e.g., Obergaulinger et al. 2010; Zrake & MacFadyen 2013).

While a generally accepted view of the process of magnetic-field amplification is still missing, broad consensus is present that the maximum achievable magnetic-field strength is reached by an equipartition between the magnetic energy and the kinetic energy on the smallest scales, thus yielding “magnetar-strength” fields of the order  $\gtrsim 10^{16}$  G (for some initial estimates, see, e.g., Price & Rosswog 2006; Liu et al. 2008; Giacomazzo et al. 2009). This expectation, which has so far been difficult to demonstrate via direct global simulations, has recently been shown to hold at least with high-resolution LES by Palenzuela et al. (2022), where the amplification of the averaged magnetic field saturated to approximately  $10^{16}$  G.

A distinct but equally interesting question is that regarding the role played by the initial magnetic-field strength and topology (for some initial investigations, see Giacomazzo et al. 2009; Kawamura et al. 2016; Ruiz et al. 2020). Following a long list of works in this area, Aguilera-Miret et al. (2022) have recently found that the initial magnetic-field topology is quickly destroyed and that the final turbulent state depends

only weakly on the configuration considered, e.g., dipoles with different strengths, misaligned dipoles, and even a multipolar structure. A common thread in all of these studies is the assumption that the magnetic fields are confined to the neutron stars and permeating the whole stellar structure. Yet, a number of works exploring the rotational, thermal, and magnetic evolution of neutron stars have considered as most natural those configurations in which the magnetic field is concentrated only in the crust (see, e.g., Pons & Geppert 2007; Pons et al. 2009). This configuration follows from assuming the stellar core as a type I superconductor that expels most of its magnetic flux on a very short timescale (see also Viganò et al. 2021). Here, we explore a BNS scenario in which, by the time of the merger, the magnetic fields in the stellar cores have been expelled or have decayed, so that only crustal fields are present. If such configurations are indeed common in neutron stars, and since the stellar crusts play a fundamental role in the development of the KHI, it is interesting to assess whether strong crustal magnetic fields lead to a distinct amplification process and to a different gravitational-wave signal.

To address this question, we report the results of high-resolution, global, and high-order GRMHD simulations of merging BNSs with two different initial magnetic-field topologies. More specifically, in addition to the standard configuration with a dipolar magnetic field filling the whole star, we consider a configuration where the magnetic field is still dipolar and has the *same* total magnetic energy but is confined to the crust only. Overall, our simulations indicate that such “crust configurations” fail to produce a sufficiently large turbulent amplification of the magnetic field and lead to a postmerger hypermassive neutron star (HMNS) with an amplified electromagnetic energy that is  $\lesssim 5\%$  of the corresponding “full configurations.”

## 2. Mathematical and Numerical Methods

The simulations reported below are obtained after solving the Einstein equations together with those of ideal GRMHD via the high-order, high-resolution, shock-capturing code `FIL` (Most et al. 2019, 2020) and the temperature-dependent equation of state `TNTYST`, which has a maximum mass of  $M_{\text{TOV}} = 2.21 M_{\odot}$  (Togashi et al. 2017). To assess whether the resolution employed is sufficient to capture the relevant physical behavior, we employ two different resolutions on the highest (seventh) refinement level with  $\Delta x \sim 0.047 M_{\odot} \approx 70$  m or of  $\Delta x \sim 0.071 M_{\odot} \approx 105$  m; we note that although these are not the highest resolutions employed so far in the literature (see, e.g., Siegel et al. 2013; Kiuchi et al. 2018), they benefit from the use of a high-order code (Most et al. 2019). Hereafter, we will refer to these two setups respectively as high (HR) and low (LR) resolutions but discuss the results of the former only; details on the LR results and their differences with the HR ones are presented in the Appendix. We note that although the resolutions employed here are very high, the magnetorotational instability (MRI) is normally underresolved for most of the matter in our simulations as estimated via different MRI quality factors (Siegel et al. 2013; Kiuchi et al. 2018). However, we expect the MRI to have little impact on the results obtained here and for two different reasons. First, the MRI would develop only in a region where  $\partial_{\varpi}\Omega < 0$ , where  $\Omega$  and  $\varpi$  are, respectively, the angular velocity and the distance from the rotation axis; however, the large shear produced at the

merger and the subsequent turbulence that follows prevent the development of a coherent angular velocity profile in the merged object at least initially. Second, because even when a coherent angular velocity profile is developed, the MRI would have the same impact on both configurations since the region where  $\partial_{\varpi}\Omega < 0$  is very similar and with comparable magnetic-field strengths in the two cases.

In both the “full configuration” and “crust configuration,” the magnetic field is initialized via the vector potential as  $A_i = A_b [-(x^j - x_{\text{NS}}^j)\epsilon_{ij}] \exp[-g_w(r - g_r)^2] \max(p - p_{\text{co}}, 0)^n$  for  $i = x, y$  and  $A_z = 0$ , where  $x_{\text{NS}}^j$  denotes the coordinate centers of the two stars ( $x_{\text{NS}}^3 = z_{\text{NS}} = 0$ ),  $r := \sqrt{\delta_{ij}(x^i - x_{\text{NS}}^i)(x^j - x_{\text{NS}}^j)}$ , and  $\epsilon_{ij}$  is the Levi-Civita symbol. The magnetized region extends outwards to the radius where the pressure reaches the cutoff pressure  $p_{\text{co}} \approx 6 \times 10^{-5} \times p_c$ , where  $p_c$  is the central pressure, and inwards to the radius  $R_{\text{in}}$ , such that  $A_i = 0$  if  $r < R_{\text{in}}$  (see Table 1 in the Appendix for additional details on the seeding parameters).

With such a prescription, the initial magnetic field has closed loops around a neutral line that is at  $\simeq 0.52 R_{\text{NS}}$  for the full configurations, while it is at  $\simeq 0.87 R_{\text{NS}}$  for the crust configurations (a view of the magnetic-field topology soon before merger is shown in Figure 5 in the Appendix). For the high (low) resolutions, the magnetized crust is resolved with  $\gtrsim 17$  ( $\gtrsim 11$ ) grid points and does not suffer from significant numerical dissipation in the remainder of the inspiral. Finally, we note that to reduce diffusion during the inspiral, the magnetic fields are seeded when the separation between the stars decreases below  $8.9 M_{\odot}$ , which corresponds to  $t - t_{\text{mer}} \lesssim -1$  ms.

## 3. Results

We start by describing the overall dynamics with particular focus on the difference between the full and crust configurations relative to the magnetic-field amplification. In the left panel of Figure 1 we report the evolution of the total electromagnetic energy in the whole computational domain  $\mathcal{V}$ ,  $E_B := \int_{\mathcal{V}} d^3x \sqrt{\gamma} (E^2 + B^2) / 8\pi$ , where  $\gamma$  is the determinant of the three metric, and  $B^2 := B_i B^i$  ( $E^2 := E_i E^i$ ) is the square modulus of the magnetic (electric) field in the Eulerian frame. The different lines refer to the crust (red) and full configurations (blue), with dashed and solid lines reporting the behavior of the LR and HR simulations, respectively. Note that all configurations start with the same electromagnetic energy of  $\sim 3 \times 10^{44}$  erg, corresponding to a maximum initial magnetic-field strength of  $\sim 10^{14}$  G ( $\sim 2.4 \times 10^{14}$  G) for the full configuration (crust configuration; see also Table 1).

To describe such complex dynamics, it is convenient to classify the evolution of  $E_B$  in four distinct stages that are highlighted by different shadings in Figure 1. The first stage of the evolution, or the “KHI-driven stage,” begins when tidal forces start significantly deforming both stars, at  $t - t_{\text{mer}} \approx -0.6$  ms ( $-0.6$ ), and ends when the KHI-driven turbulence ceases to increase  $E_B$  at  $t - t_{\text{mer}} \approx 2.46$  ms (0.9) for the full (crust) configuration.<sup>7</sup> The KHI-unstable shear layer can be seen in the first column of Figure 2, which presents cross sections of the norm of the magnetic field  $|B| := \sqrt{B^i B_i}$  in the

<sup>7</sup> A more careful examination of Figures 1 and 2 reveals that there are two different phases in the KHI-driven stage with slightly different growth rates; for simplicity, we will ignore these small differences.

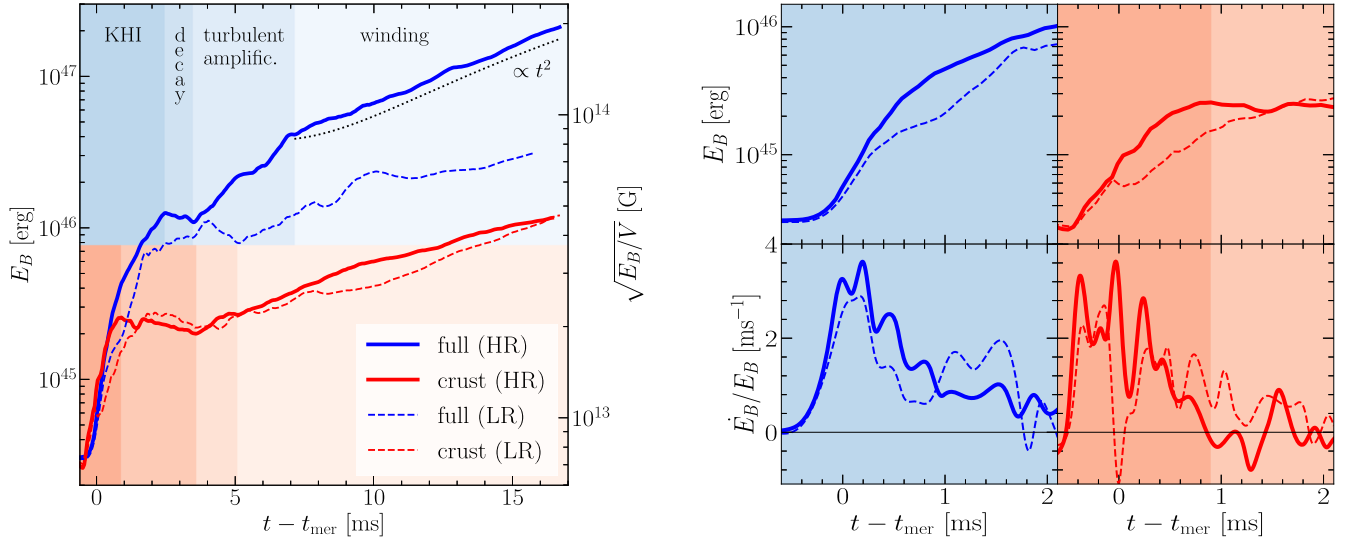


**Figure 1.** Left: evolution of the total magnetic energy  $E_B$  for the HR full (blue solid line) and crust configurations (red solid line); dashed blue (red) lines refer to the LR full and crust configurations, respectively. Different shadings highlight the four stages of the evolution. The black dotted line shows a quadratic fit to full (HR) in the winding stage and is shifted downwards for better visualization. The quantity  $V$  denotes the reference volume of a sphere with a radius of 11 km. Right top row of right panel: the same as in the left panel but for  $t - t_{\text{mer}} \lesssim 2$  ms. Right panel, bottom row: the same as the top row of the right panel but for the growth rate  $\dot{E}_B/E_B$ .

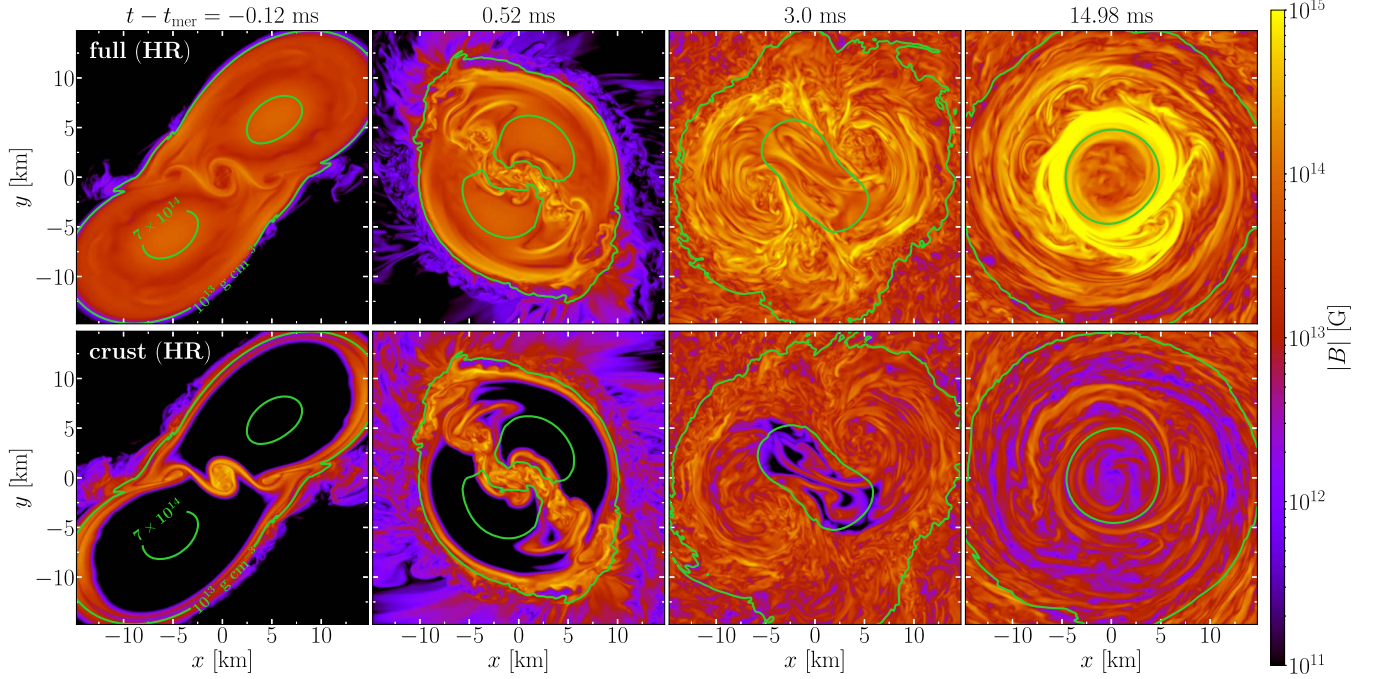


**Figure 2.** Distributions on the  $(x, y)$  plane of the magnetic-field strength  $|B|$  from the HR simulations at four representative times. The top and bottom rows refer to the full and crust configurations, respectively.

$(x, y)$ -plane at time  $t - t_{\text{mer}} = -0.12$  ms and at an elevation<sup>8</sup> of  $z \simeq 1 \text{ km} \lesssim 0.115 R_{\text{NS}}$  for the full (top row) and crust configurations (bottom row). The second column of Figure 2, at  $t - t_{\text{mer}} = 0.52$  ms, highlights how the KHI-driven turbulent motion at the interface between the stars extends to other regions and involves also the stellar interiors. At this point, the amplification of the magnetic field has almost ended for the crust configuration, as can be appreciated from the left panel of Figure 1.

<sup>8</sup> We use this elevation to minimize the influence of the boundary conditions across the equatorial plane; smaller elevations yield very similar views.

The second stage of the evolution, or “decay stage,” is characterized by a lack of amplification, and the evolution of  $E_B$  is constant in time or exhibits a weak decay. This is the result of a combination of factors: the expansion of the dense HMNS core ( $\rho \gtrsim 10^{13} \text{ gm/cm}^3$ ), the ejection of matter at the HMNS surface, and an insufficient magnetic-field amplification. During this stage, magnetic pressure gradients accelerate the expansion of matter in the remnant and hence are doing work on the fluid. At the same time, the KHI-driven turbulent motion ceases to be produced efficiently as the kinetic energy in the remnant is reduced through the emission of gravitational waves, shock-heating, and matter ejection. This leads to an overall decrease in the electromagnetic energy. It is interesting



to note that during this stage, the lack of turbulence in the HMNS core results in the magnetic fields of the crust configurations to remain very weak and the full configuration to preserve its initial large-scale coherence; this can be seen in the third column of Figure 2 at  $t - t_{\text{mer}} = 3$  ms. The decay stage ends for the full (crust) configuration at  $t - t_{\text{mer}} = 3.48$  ms (3.59).

The third stage, or “turbulent-amplification stage,” is characterized by a new process of magnetic-field amplification that becomes strong enough to counteract the decay of the previous stage and leads to a net amplification (see also the high-resolution calculations of Siegel et al. 2013). At this point in the evolution, the HMNS has emerged from the highly nonlinear, early postmerger phase in which the two stellar cores collide and bounce (see Takami et al. 2015 for a toy model). Subsequent turbulent motions can develop and lead to a nonlinear amplification of the magnetic field—with a smaller growth rate than in the KHI stage and not related to the development of the MRI—that result into a substantial growth of the poloidal field up to  $t - t_{\text{mer}} = 7.13$  ms (5.09).

The fourth and final stage, or “winding stage,” starts when the turbulence is fully developed and more regular, large-scale shearing motions can be produced in the HMNS. Under the infinite-conductivity conditions of ideal MHD, these motions lead to the well-known linear-in-time growth of the magnetic field that represents the quasistationary state reached in our simulations (see the final part of the simulations shown in the left panel of Figure 1 and the fourth column of Figure 2). Obviously, the winding stage cannot continue indefinitely but will terminate when the magnetic-field energy is in equipartition with the kinetic energy stored in the differential rotation so that further amplification is energetically disfavored. We should note that the classification discussed here describes well the dynamics in our simulations, which have moderate initial magnetic fields. However, if the initial exponential amplification is much larger—as a result of additional driving terms in the MHD equations (Giacomazzo et al. 2015; Palenzuela et al. 2022) or of very large initial magnetic fields (Kiuchi et al. 2018)—equipartition may be reached much earlier, and the subsequent stages may be absent (for where these stages are not found, see Giacomazzo et al. 2015; Kiuchi et al. 2018; Palenzuela et al. 2022).

While the dynamics and stage classification presented so far applies to both crust and full configurations, important differences are present that ultimately determine the final magnetic-field amplification. In particular, the KHI-driven evolution is very efficient in the crust configuration but also ends earlier than for the full configuration, thus achieving a smaller magnetic-field amplification. In addition, the KHI is followed by a longer decay stage and a shorter turbulent amplification (see red solid line in the left panel of Figure 1). As a result, when the winding stage starts for the crust configuration, the magnetic energy is about 1 order of magnitude smaller than in the full configuration; since the growth rates are comparable in the two topologies, this difference remains unchanged until the end of the simulations. Also worth noting is that the turbulent amplification is smaller in the crust configuration as the result of two combined effects. First, a smaller amount of magnetized matter is subject to turbulent motions. Second, because the magnetized matter is only at lower densities (i.e.,  $\rho \lesssim 10^{13}$  gm/cm<sup>3</sup>) and near the stellar surface, a good portion of it is shed in the external

medium before it can be amplified further. These “winds,” that are in good part (but not exclusively) magnetically driven, are the result of large deviations from a magnetohydrostatic equilibrium at the remnant surface and are made more violent by the presence of comparatively stronger magnetic fields in the crust configuration. By contrast, the amplification in the full configuration can benefit from larger volumes of magnetized matter and smaller losses of magnetized matter at the surface, where the pressure gradients are comparatively smaller.

The right panel of Figure 1 gives us the opportunity to discuss in more detail the turbulent magnetic-field amplification during the first two stages of the evolution and thus for  $t - t_{\text{mer}} \lesssim 2$  ms. In particular, shown in the upper parts is the evolution of  $E_B$  for the same configurations in the left panel, while the lower parts report the corresponding normalized growth rate  $\dot{E}_B/E_B$ . First, an exponential growth is present at the onset of magnetic-field amplification, which then reaches its maximum value in  $\lesssim 0.2$  ms (0.7) for the crust (full) configuration. While the maximum growth rates of the two configurations are comparable for the same resolution, the changes in  $E_B$  are considerably more rapid in the crust configuration, as it is natural to expect since the magnetic energy involved in the KHI amplification is confined to a smaller volume and nearly all of the initial electromagnetic energy participates in the amplification process as the KHI develops. After the maximum of  $\dot{E}_B/E_B$  has been reached, the subsequent evolution is qualitatively very similar in all configurations. In particular, the growth rate decays until it reaches negative values and the KHI-driven stage ends. During this decay, very short variations of the growth rate take place with a period of  $\simeq 0.25$ – $0.35$  ms; considering an eddy-rotation velocity of  $\sim 0.15 c$ , this variation yields eddy length scales of  $\sim 1.8$ – $2.5$  km, which match well the size of the largest eddies produced across all simulations. This suggests that the decay in the growth rate is related to the largest eddy turnovers in the KHI-driven stage, and the periodic increase/decrease of the growth rate is the result of the amplification and subsequent dissipation of large-scale flux tubes that are dragged into rotation by the largest eddies. Furthermore, due to periodic bounces of the two cores with a period of  $\sim 0.77$  ms, the shear layer between the stars is turned over at half of this period and drives the production of the largest eddies. This dynamics highlights that a persistent amplification requires the development of a fully turbulent stellar interior. While this is almost inevitable in the case of the full configuration, where magnetized material is present across the HMNS, continued amplification is difficult for the crust configuration, where turbulent amplification is still present, but it is accompanied by the mixing of magnetized and unmagnetized material. Such mixing, in addition to magnetized-matter losses at the HMNS surface, reduces the growth rate and favors dissipation.

Figure 3 offers an alternative means of comparing the full (top row) and crust configurations (bottom row) in the KHI-driven stage by examining representative quantities at  $t - t_{\text{mer}} = 0.52$  ms. From left to right we report:  $|B|/[10^{15} \text{ G}]$ ; the kinematic vorticity  $|\rho\omega_{\perp}^{\text{xy}}| := \rho h_{\mu}^x h_{\nu}^y \omega^{\mu\nu}$ ; and the amplification source term,  $s_{\text{mag}} := b^{\mu} b^{\nu} \sigma_{\mu\nu} - b^2 \Theta/6$ . Here  $h_{\nu}^{\mu}$  denotes the projector tensor onto spatial hypersurfaces in the  $3 + 1$  formalism (Rezzolla & Zanotti 2013),  $\omega^{\mu\nu}$  the kinematic vorticity,  $b^{\mu}$  the magnetic field in the fluid frame,  $\sigma_{\mu\nu}$  the shear tensor, and  $\Theta$  the expansion scalar (see Chabanov et al. 2021 for definitions). The quantity  $s_{\text{mag}}$  is the general-relativistic

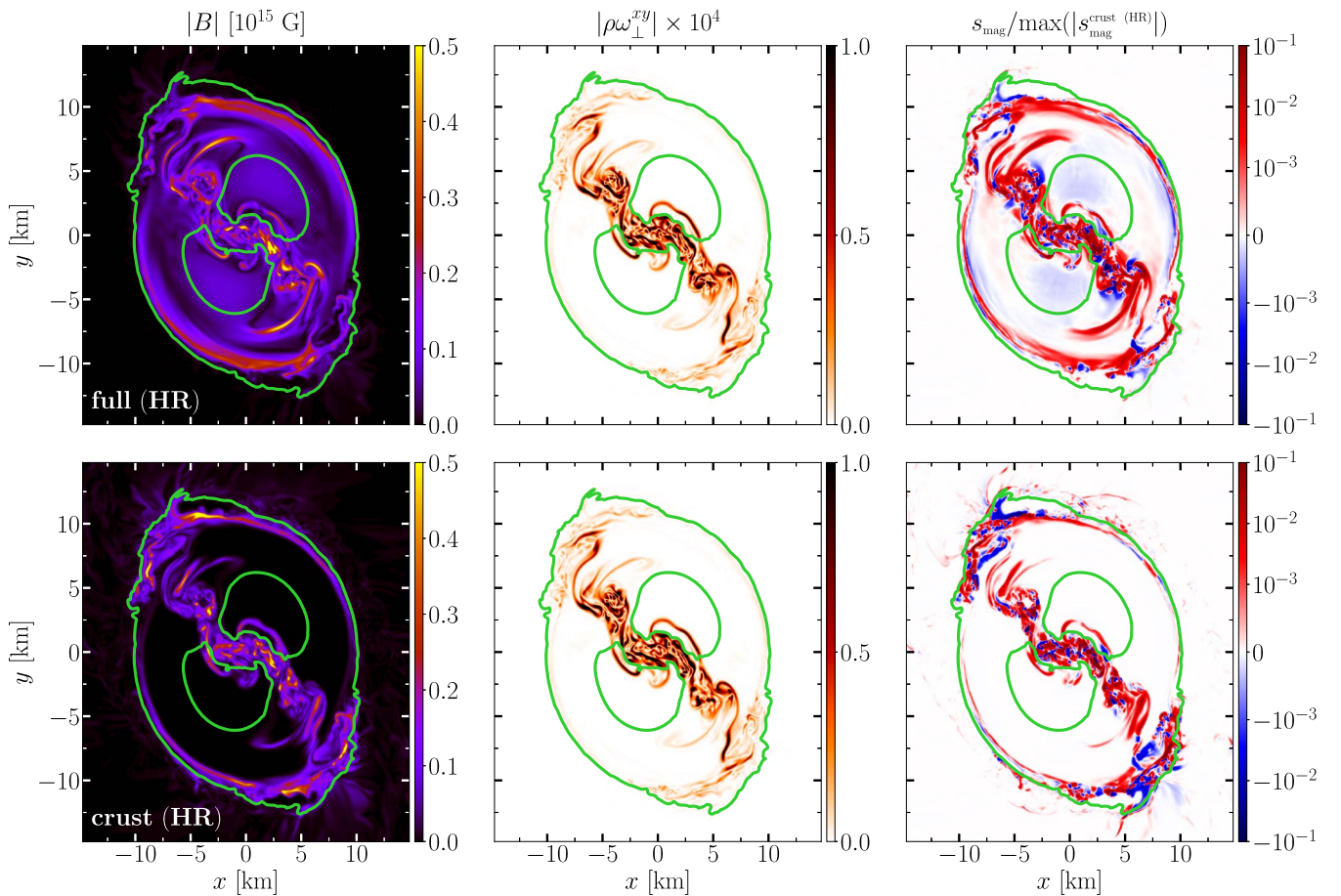


**Figure 3.** Distributions on the  $(x, y)$  plane of the magnetic-field strength  $|B|$  (left column), of the density-weighted  $xy$ -component of the kinematic vorticity  $|\rho\omega_{xy}|$  (middle column), and of the amplification source term  $s_{\text{mag}}$  (right column) at  $t - t_{\text{mer}} = 0.52$  ms. The top and bottom rows refer to the full and crust configurations, respectively.

counterpart of the quantity employed by Obergaulinger et al. (2010) to measure the strength of local sources ( $s_{\text{mag}} > 0$ ) and sinks ( $s_{\text{mag}} < 0$ ) of electromagnetic energy.

First, when comparing  $|B|$  between the two configurations (left column), it is apparent that the largest values of the magnetic-field strength can be found in the crust configuration and that these are reached very close to the putative surface of the HMNS (marked with a green contour line at  $10^{13}$  gm/cm<sup>3</sup>), while the inner parts are essentially devoid of magnetic field with the exception of those regions that belonged to the stellar surface. Second, when looking at the vorticity (middle column), it also clear that the difference between the two configurations is very small and that in both cases the turbulent motion is concentrated in the low-density regions and falls off rapidly when moving toward the stellar interior where, again, the turbulence is present only in the regions which were on the stellar surface. Finally, when comparing the sources and sinks of magnetic energy (right column), it is possible to realize that in both cases the sources are larger than the sinks (hence the amplification) but also that a large portion of the sources in the crust configuration is just about to be lost at the HMNS surface. It is exactly the shedding of this precious, highly magnetized material that will quench the further amplification of the crust configuration and ultimately lead to smaller magnetic fields. The emission of neutrinos may further increase the strength of these winds, thus additionally reducing the potential of magnetic-field amplification in crust configurations.

We conclude our analysis by discussing the impact that the different magnetic-field topologies have on the emitted gravitational-wave signal, which we report in Figure 4. Note that the signals from the two configurations are indistinguishable during the inspiral and very similar over the first 2 ms after the merger, when the KHI is most active. However, after  $t - t_{\text{mer}} \gtrsim 2$  ms the waveforms differ considerably both in phase and amplitude, with the latter being smaller for the full configuration. This is because the production of magnetic fields comes at the cost of the kinetic energy of the system in the full configuration. In addition, the strong amplification of the magnetic field in the full configuration reduces the  $m=2$  deformations, leading to a more axisymmetric HMNS in the full configuration and hence to a weaker gravitational-wave signal.

#### 4. Conclusions

Motivated by a commonly assumed scenario in which magnetic fields in neutron stars are confined to a small region near the stellar surface, we have performed high-resolution, global, and high-order GRMHD simulations of merging BNSs with different initial magnetic-field topologies. In particular, while keeping the magnetic energy the same, we have investigated the impact of a purely *crustal* magnetic field and contrasted it with the standard configuration consisting of a dipolar magnetic field filling the whole star.

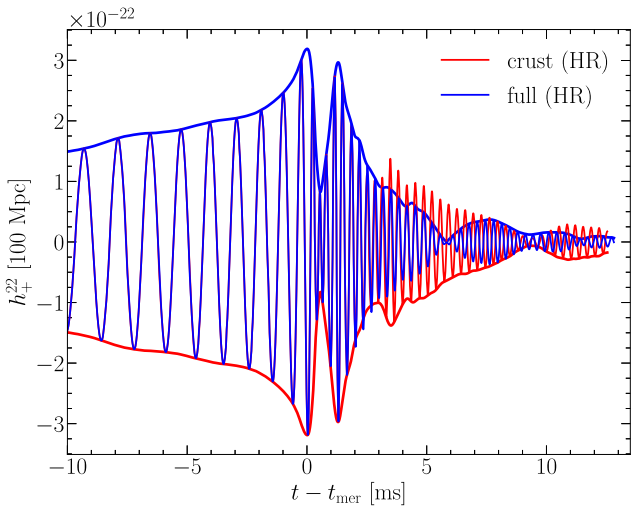


**Figure 4.** Gravitational-wave strain in the  $\ell=2$ ,  $m=2$  mode of the  $+-$  polarization extracted at  $\sim 740$  km for a source at and normalized to a distance of 100 Mpc and for the two configurations. Thick solid lines report the corresponding amplitudes.

The use of high spatial resolution, high-order methods and realistic initial magnetic fields has allowed us to highlight the presence of four distinct stages in the evolution of the magnetic field. While these stages are common to both configurations, and although the crust configurations are more efficient in generating strong magnetic fields during the KHI-driven stage, we find that crust configurations fail to achieve the same level of magnetic-field amplification as their full counterparts. We attribute this behavior to the lack of magnetized material in the neutron-star interiors that can be used for further amplification and to the losses at the stellar surface of highly magnetized matter that afflicts the crust configurations. As a result, by the end of our simulations the magnetic energies in the two configurations differ by a bit more than 1 order of magnitude, and the gravitational-wave signal in the full configuration is  $\sim 50\%$  weaker than in the crustal counterpart as a result of a larger degree of axisymmetry.

Inevitably for global, fully general-relativistic simulations of this type, ours also suffers from resolutions that, while very high and computationally expensive, are insufficient to capture a fully convergent behavior during the KHI-driven exponential growth. However, by performing simulations with different resolutions, we have verified that the behavior presented here is only quantitatively modified by resolution and that the qualitative features remain unaltered. Hence, we expect our results to provide a reasonably accurate description of the magnetic-field amplification for stars with realistic initial magnetic fields.

Our findings have at least two important implications. First, future observations providing evidence for the presence of magnetar-strength magnetic fields in the merger remnant will represent a clear indication that the magnetic-field topology before the merger could not have been a purely crustal one. Second, since the main difference between the two configurations considered here is represented by the volume fraction endowed with magnetic field, it is possible to correlate the postmerger dynamics—both in terms of gravitational-wave emission and in ejected matter—to the fraction of stellar volume that is magnetized. We leave these investigations to future work.

We thank Vasilis Mpsketzis for useful discussions. Partial funding comes from the GSI Helmholtzzentrum für Schwerionenforschung, Darmstadt as part of the strategic R&D collaboration with Goethe University Frankfurt, from the State of Hesse within the Research Cluster ELEMENTS (Project ID 500/10.006), by the ERC Advanced Grant “JETSET: Launching, propagation and emission of relativistic jets from binary mergers and across mass scales” (grant No. 884631) and the Deutsche Forschungsgemeinschaft (DFG, German Research Foundation) through the CRC-TR 211 “Strong-interaction matter under extreme conditions”—project number 315477589—TRR 211. L.R. acknowledges the Walter Greiner Gesellschaft zur Förderung der physikalischen Grundlagenforschung e.V. through the Carl W. Fueck Laureatus Chair. The simulations were performed on HPE Apollo HAWK at the High Performance Computing Center Stuttgart (HLRS) under the grant BNSMIC. E.R.M. gratefully acknowledges support as the John A. Wheeler Fellow at the Princeton Center for Theoretical Science, the Princeton Gravity Initiative and the Institute for Advanced Study. E.R.M. acknowledges support through the Extreme Science and Engineering Discovery Environment (XSEDE) through Expanse at SDSC and Bridges-2 at PSC through allocations PHY210053 and PHY210074. E.R.M. further acknowledges supported by Princeton Research Computing, a consortium of groups including the Princeton Institute for Computational Science and Engineering (PICSciE) and the Office of Information Technology’s High Performance Computing Center and Visualization Laboratory at Princeton University.

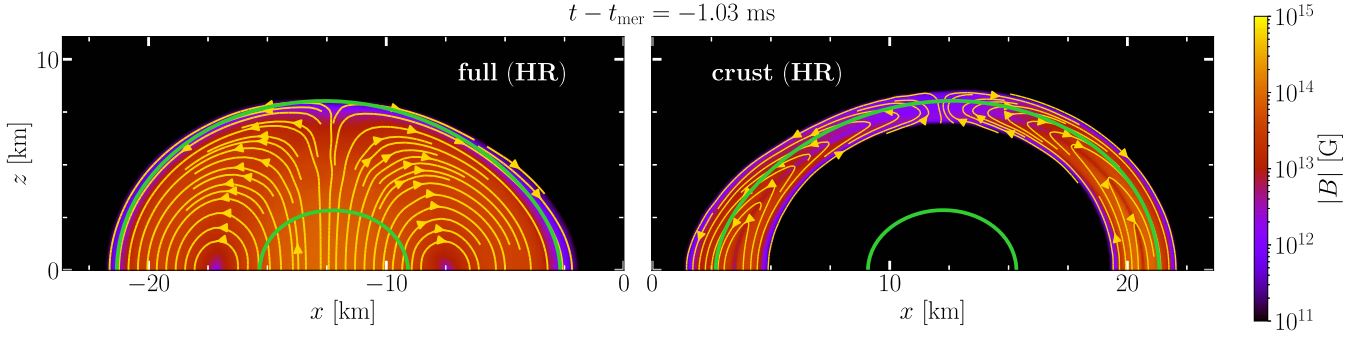
*Software:* Einstein Toolkit (Löffler et al. 2012), Carpet (Schnetter et al. 2004), FIL (Most et al. 2019), FUKA (Papenfort et al. 2021), Kadath (Grandclement 2010), CompOSE (<https://compose.obspm.fr>).

## Appendix Simulation Details and Impact of Resolution

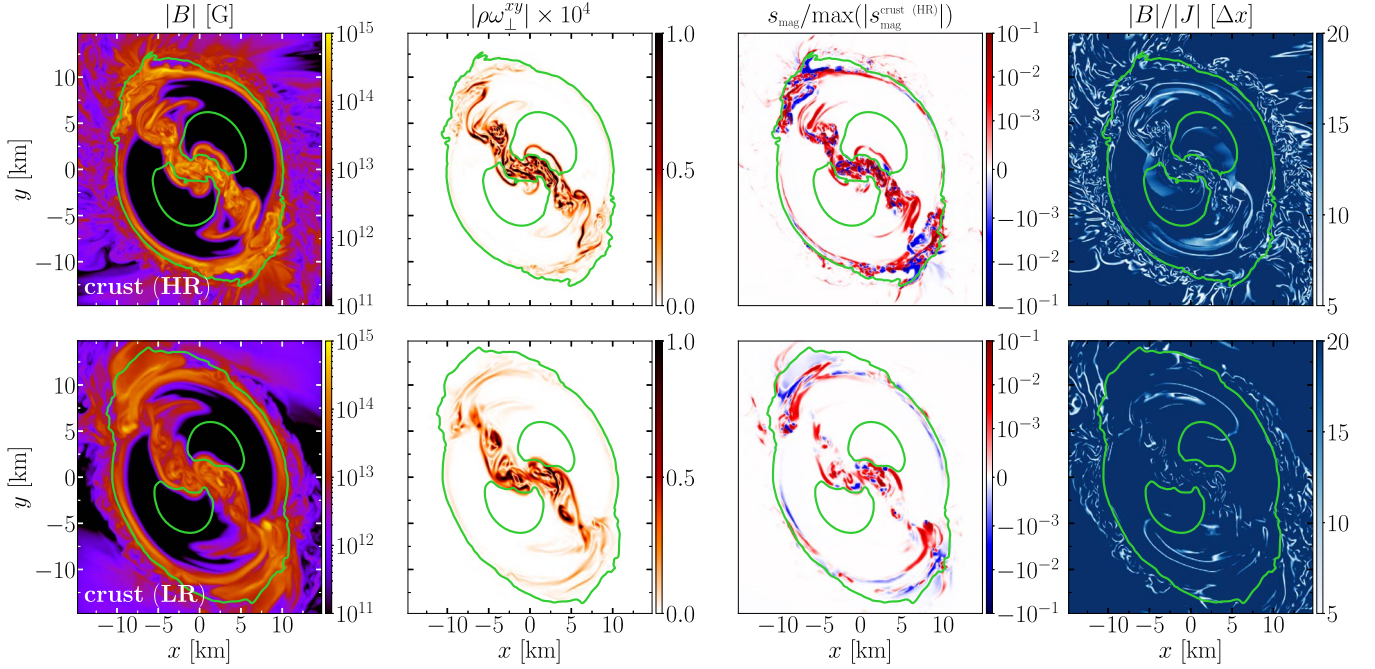
In what follows we provide additional details on the features of the simulations reported in the main text, as well as a discussion of how the amplification differs when considering lower resolutions. In particular, we recall that the simulations have been performed with the FIL code, which employs fourth-order accurate finite-difference stencils in Cartesian coordinates for the evolution of the constraint damping formulation of the Z4 formulation of the Einstein equations (Bernuzzi & Hilditch 2010; Alic et al. 2012), while the equations of GRMHD are solved with a fourth-order high-resolution shock-capturing scheme (Del Zanna et al. 2007), together with a vector-potential-based constrained transport scheme inherited from the open-source code IllinoisGRMHD (Etienne et al. 2015). On the other hand, initial data is computed using the FUKA codes (Papenfort et al. 2021) where the equal-mass binaries are chosen to be irrotational with a total Arnowitt–Deser–Misner mass of  $\sim 2.55 M_{\odot}$  initialized at a separation of  $\sim 30 M_{\odot} \approx 44$  km. The computational grid has outer boundaries at  $1000 M_{\odot} \approx 1476$  km in the three spatial directions, and we employ a  $z$ -symmetry in the equatorial plane. We use seven refinement levels with factor of 2 refinement; the last level, which has a width of  $32 M_{\odot}$ , is added prior to merger, when the separation between the “barycenters” of the two stars is  $\lesssim 9 M_{\odot}$ .

Table 1 reports the smallest employed cell size  $\Delta x$ , the parameters of the initial magnetic field, and the initial





**Figure 5.** Distributions on the  $(x, z)$  plane of the magnetic-field strength  $|B|$  from the HR simulations soon before merger. Magnetic-field lines are shown in yellow, while the left and right panels refer to the full and crust configurations, respectively.



**Figure 6.** The first three columns from left are the same as in Figure 3, while the fourth column reports the characteristic length scale of the magnetic field, i.e.,  $|B|/|J|$ , when expressed in units of resolution spacing  $\Delta x$ .

maximum magnetic-field strength  $|B|_{\max}^{\text{seed}}$ . Also reported are the times characterizing the different stages of our simulations, namely, the end of the KHI-driven stage  $t_{\text{end}}^{\text{KHI}}$ , the end of the decay stage  $t_{\text{end}}^{\text{D}}$ , and the end of the turbulent-amplification stage  $t_{\text{end}}^{\text{TA}}$ .

In analogy with Figure 2, we use Figure 5 to offer a more intuitive view of the different topologies of the magnetic field also on the  $(x, z)$  plane. In particular, the figure reports the distributions of the magnetic-field strength  $|B|$  from the HR simulations soon before merger. Magnetic-field lines are shown in yellow, while the left and right panels refer to the full and crust configurations, respectively; note that in both cases the magnetic field is purely poloidal.

Next, and in addition to what is already presented in Figure 1, we discuss how the resolution impacts our results by contrasting the LR and HR versions of the crust configuration (we do not concentrate here on the full configurations as these show very similar behavior for both resolutions so that the discussion on full (HR) is applicable to full (LR); also these have been discussed in a number of papers, e.g., see Most et al. (2019) for a case with lower resolutions and higher magnetic-

field strengths compared to the simulations in this work). Bearing in mind that the resolutions employed here do not allow for a rigorous convergence study, the overall evolution of the LR and HR simulations provides evidence of being numerically consistent, i.e., that the errors should decrease with resolution. More specifically, Figure 6 compares the HR (top row) at  $t - t_{\text{mer}} = 0.52$  ms with the LR simulations (bottom row) at  $t - t_{\text{mer}} = 0.59$  ms, where the different times are due to the difference in phase evolution due to the different resolution. The first three columns from the left report the same quantities as shown in Figure 3. The fourth column, on the other hand, reports the characteristic length scale of the magnetic field, i.e.,  $|B|/|J|$ , when expressed in units of resolution spacing  $\Delta x$  (see Equation (15) of Obergaulinger et al. 2010). Here,  $J := \sqrt{J^i J_i}$  and the spatial current is estimated as

$$J^i \simeq \frac{1}{4\pi\alpha} \epsilon^{ijk} D_j (\alpha B_k). \quad (1)$$

Expression (1) follows from the fact that in ideal GRMHD, the spatial components of the electric field can be expressed as

**Table 1**  
Characterizing Information on the Different Models Explored in This Work





Model	$\Delta x$ (m)	$R_{in}$ ( $M_{\odot}$ )	$A_b$	$g_w$ ( $M_{\odot}^{-2}$ )	$g_r$ ( $M_{\odot}$ )	$P_{co}$ ( $M_{\odot}^{-2}$ )	$n$	$ B _{max}^{seed}$ (G)	$t_{end}^{KHI} - t_{mer}$ (ms)	$t_{end}^D - t_{mer}$ (ms)	$t_{end}^{TA} - t_{mer}$ (ms)
full (HR)	70	0	0.028	0	0.0	$1.0 \times 10^{-8}$	1.00	$1.04 \times 10^{14}$	2.46	3.48	7.13
full (LR)	105	0	0.028	0	0.0	$1.0 \times 10^{-8}$	1.00	$1.04 \times 10^{14}$	1.77	5.15	10.1
crust (HR)	70	5	0.131	4	6.1	$1.0 \times 10^{-8}$	0.85	$2.36 \times 10^{14}$	0.90	3.59	5.09
crust (LR)	105	5	0.120	4	6.1	$1.6 \times 10^{-7}$	0.85	$2.26 \times 10^{14}$	1.82	3.54	11.5

**Note.** We show the cell size on the highest refinement level; the seed magnetic-field parameters employed to initialize the magnetic field; the maximum magnetic-field strength after initialization,  $|B|_{max}^{seed}$ ; as well as the end time of the different stages discussed in the text, i.e.,  $t_{end}^{KHI}$ ,  $t_{end}^D$ , and  $t_{end}^{TA}$ , respectively.

$\alpha E_i = -\epsilon_{ijk}(v^j + \beta^j)B^k$  so that for nonrelativistic flows,  $E_i \sim \mathcal{O}(v_i) \ll 1$ , and the current reduces to Equation (1).

Starting from the first column of Figure 6 it is possible to realize that the HR simulation loses more magnetized material across the HMNS surface than the LR counterpart. This loss is most significant at both ends of the turbulent shear layer where also dynamical ejecta will originate from. The second column compares the densitized vorticity and shows that, as expected, more vorticity is present in the HR simulation and that the differences are more marked at both ends of the turbulent interface. The third column shows that stronger sinks (higher in magnitude but negative) are present at the ends of the turbulent interface in the HR simulation. Finally, the fourth column clearly shows that the HMNS in the HR simulation is surrounded by a “cloud” of low-density and magnetized material with a very small characteristic length scale, which is not visible in the LR simulation. All in all, Figure 6 illustrates how higher resolution for the crust configuration can lead to enhanced shedding of highly magnetized material at the HMNS surface and hence that the magnetic-field amplification is bound to be smaller as opposed to the full configuration.

### ORCID iDs

Michail Chabanov  <https://orcid.org/0000-0001-9676-765X>  
 Samuel D. Tootle  <https://orcid.org/0000-0001-9781-0496>  
 Elias R. Most  <https://orcid.org/0000-0002-0491-1210>  
 Luciano Rezzolla  <https://orcid.org/0000-0002-1330-7103>

### References

- Abbott, B. P., Abbott, R., Abbott, T. D., et al. 2017, *PhRvL*, **119**, 161101  
 Aguilera-Miret, R., Viganò, D., Carrasco, F., Miñano, B., & Palenzuela, C. 2020, *PhRvD*, **102**, 103006  
 Aguilera-Miret, R., Viganò, D., & Palenzuela, C. 2022, *ApJL*, **926**, L31  
 Alic, D., Bona-Casas, C., Bona, C., Rezzolla, L., & Palenzuela, C. 2012, *PhRvD*, **85**, 064040  
 Anderson, M., Hirschmann, E. W., Lehner, L., et al. 2008, *PhRv*, **100**, 191101  
 Bernuzzi, S., & Hilditch, D. 2010, *PhRvD*, **81**, 084003  
 Chabanov, M., Rezzolla, L., & Rischke, D. H. 2021, *MNRAS*, **505**, 5910  
 Ciolfi, R. 2020a, *MNRAS*, **495**, L66  
 Ciolfi, R. 2020b, *GRGr*, **52**, 59  
 Cowperthwaite, P. S., Berger, E., Villar, V. A., et al. 2017, *ApJL*, **848**, L17  
 Del Zanna, L., Zanotti, O., Bucciantini, N., & Londrillo, P. 2007, *A&A*, **473**, 11  
 Drout, M. R., Piro, A. L., Shappee, B. J., et al. 2017, *Sci*, **358**, 1570  
 Etienne, Z. B., Paschalidis, V., Haas, R., Mösta, P., & Shapiro, S. L. 2015, *CQGra*, **32**, 175009  
 Fernández, R., Tchekhovskoy, A., Quataert, E., Foucart, F., & Kasen, D. 2019, *MNRAS*, **482**, 3373  
 Fujibayashi, S., Kiuchi, K., Wanajo, S., et al. 2023, *ApJ*, **942**, 39  
 Giacomazzo, B., Rezzolla, L., & Baiotti, L. 2009, *MNRAS*, **399**, L164  
 Giacomazzo, B., Rezzolla, L., & Baiotti, L. 2011, *PhRvD*, **83**, 044014  
 Giacomazzo, B., Zrake, J., Duffell, P. C., MacFadyen, A. I., & Perna, R. 2015, *ApJ*, **809**, 39  
 Gottlieb, O., Moseley, S., Ramirez-Aguilar, T., et al. 2022, *ApJL*, **933**, L2  
 Grandclement, P. 2010, *JCoPh*, **229**, 3334  
 Kawamura, T., Giacomazzo, B., Kastaun, W., et al. 2016, *PhRvD*, **94**, 064012  
 Kiuchi, K., Cerdá-Durán, P., Kyutoku, K., Sekiguchi, Y., & Shibata, M. 2015a, *PhRvD*, **92**, 124034  
 Kiuchi, K., Sekiguchi, Y., Kyutoku, K., et al. 2015b, *PhRvD*, **92**, 064034  
 Kiuchi, K., Kyutoku, K., Sekiguchi, Y., & Shibata, M. 2018, *PhRvD*, **97**, 124039  
 Kiuchi, K., Kyutoku, K., & Shibata, M. 2012, *PhRvD*, **86**, 064008  
 Liu, Y. T., Shapiro, S. L., Etienne, Z. B., & Taniguchi, K. 2008, *PhRvD*, **78**, 024012  
 Löffler, F., Faber, J., Bentivegna, E., et al. 2012, *CQGra*, **29**, 115001  
 Most, E. R., Jens Papenfort, L., Dexheimer, V., et al. 2020, *EPJA*, **56**, 59  
 Most, E. R., Papenfort, L. J., & Rezzolla, L. 2019, *MNRAS*, **490**, 3588  
 Murguía-Berthier, A., Ramirez-Ruiz, E., Montes, G., et al. 2016, *ApJL*, **835**, L34  
 Nathanail, A., Gill, R., Porth, O., Fromm, C. M., & Rezzolla, L. 2020, *MNRAS*, **495**, 3780  
 Nathanail, A., Gill, R., Porth, O., Fromm, C. M., & Rezzolla, L. 2021, *MNRAS*, **502**, 1843  
 Obergaulinger, M., Aloy, M. A., & Müller, E. 2010, *A&A*, **515**, A30  
 Palenzuela, C., Aguilera-Miret, R., Carrasco, F., et al. 2022, *PhRvD*, **106**, 023013  
 Palenzuela, C., Lehner, L., Ponce, M., et al. 2013, *PhRvL*, **111**, 061105  
 Palenzuela, C., Liebling, S. L., Neilsen, D., et al. 2015, *PhRvD*, **92**, 044045  
 Papenfort, L. J., Tootle, S. D., Grandclement, P., Most, E. R., & Rezzolla, L. 2021, *PhRv*, **104**, 024057  
 Pons, J. A., & Geppert, U. 2007, *A&A*, **470**, 303  
 Pons, J. A., Miralles, J. A., & Geppert, U. 2009, *A&A*, **496**, 207  
 Price, D. J., & Rosswog, S. 2006, *Sci*, **312**, 719  
 Radice, D. 2017, *ApJL*, **838**, L2  
 Rezzolla, L., Giacomazzo, B., Baiotti, L., et al. 2011, *ApJL*, **732**, L6  
 Rezzolla, L., & Zanotti, O. 2013, *Relativistic Hydrodynamics* (Oxford: Oxford Univ. Press)  
 Ruiz, M., Tsokaros, A., & Shapiro, S. L. 2020, *PhRvD*, **101**, 064042  
 Schnetter, E., Hawley, S. H., & Hawke, I. 2004, *CQGra*, **21**, 1465  
 Siegel, D. M., Ciolfi, R., Harte, A. I., & Rezzolla, L. 2013, *PhRvD*, **87**, 121302  
 Takami, K., Rezzolla, L., & Baiotti, L. 2015, *PhRvD*, **91**, 064001  
 Togashi, H., Nakazato, K., Takehara, Y., et al. 2017, *NucPh*, **A961**, 78  
 Viganò, D., Garcia-Garcia, A., Pons, J. A., Dehman, C., & Graber, V. 2021, *CoPhC*, **265**, 108001  
 Zrake, J., & MacFadyen, A. I. 2013, *ApJ*, **769**, L29